Scientific Reports

https://doi.org/10.1038/s41598-025-30897-3

Article in Press

# Sensitive detection of cancer and brain tissues using a miniaturized PT-symmetric nanophotonic biosensor based on exceptional points

Received: 24 September 2025

Accepted: 27 November 2025

Published online: 05 December 2025

Cite this article as: Mohammadpour A., Vala A.S. & Barvestani J. Sensitive detection of cancer and brain tissues using a miniaturized PT-symmetric nanophotonic biosensor based on exceptional points. *Sci Rep* (2025). https://doi.org/10.1038/s41598-025-30897-3

Ali Mohammadpour, Ali Soltani Vala & Jamal Barvestani

# Sensitive Detection of Cancer and Brain Tissues Using a Miniaturized PT-Symmetric Nanophotonic Biosensor Based on Exceptional Points

Ali Mohammadpour[1], Ali Soltani Vala, Jamal Barvestani

*Faculty of Physics, University of Tabriz, Tabriz 51666-16471, Iran.*

***Abstract.*** *In this study, a one-dimensional nanophotonic biosensor is introduced for the detection of cancer cells and tissues. The investigation focuses on three distinct multilayer structures designated $S_1$, $S_2$, and $S_3$ each characterized by unique symmetry properties. While $S_1$ and $S_2$ exhibit parity-time (PT) symmetry, $S_3$, a hybrid configuration, demonstrates augmented parity-time (APT) symmetry. The sensing mechanism is based on the appearance of exceptional points (EPs) in response to the presence of analytes, facilitating their precise and sensitive identification. Under identical operational conditions, three key phenomena are observed. First, by locating the exceptional point and utilizing the bidirectional transparency phenomenon, the structural parameters are optimized to maximize transmission at the refractive index corresponding to cancer cells and tissues. This enables accurate diagnosis by correlating the analyte's refractive index with the EP. Second, in structure $S_3$, a reduction in both layer thickness and porosity ratio results in a miniaturization effect, underscoring the influence of structural downsizing. Third, the implementation of APT symmetry in $S_3$ reduces the number of sampling parameters, enabling a more efficient and minimalistic sampling approach, referred to as a minor sampling technique. This approach minimizes the sample volume required for effective detection while maintaining measurement accuracy, offering promising implications across various sensing applications. As a whole, these outcomes propose a novel strategy for the identification of cell and tissue types through the exploitation of exceptional points, an area previously underexplored. Furthermore, the synergy between the miniaturization effect and an optimized sampling approach, significantly advances the prospects for developing high-precision biosensors.*

***Keywords.*** *Bidirectional Transparency, Biosensor, Brain Tissues, Cancer Cells, Exceptional Points, Miniaturization, Minor Sampling, Parity-Time Symmetry.*

[1] Corresponding author: a.m.pour@tabrizu.ac.ir

## Introduction

Recent studies have increasingly concentrated on light–matter interactions and the tunable control of electromagnetic wave propagation within sensitive medium layers embedded in photonic crystal structures [1, 2, 3, 4, 5, 6, 7, 8, 9, 10]. Owing to their high sensitivity and broad range of applications, optical sensors based on parity-time (PT) symmetry have attracted considerable interest. PT-symmetric non-Hermitian systems are characterized by spatially balanced distributions of optical gain and loss, where the refractive index (RI) profile satisfies the PT-symmetry condition: $n(\vec{r}) = n^*(-\vec{r})$. The real part of the RI exhibits even symmetry, while the imaginary part exhibits odd symmetry with respect to the spatial coordinate [11, 12, 13, 14, 15]. In contrast to conventional PT-symmetric configurations, which rely on global balance between spatially separated gain and loss layers, the augmented PT (APT) symmetry introduced in this work incorporates local symmetry within each unit cell. This structural modification produces a dual-level symmetry, both at the layer and the unit-cell scale leading to stronger mode coupling and earlier occurrence of exceptional points under reduced geometrical thickness. Such an internal symmetry not only minimize the total footprint of the biosensor but also enhances its sensitivity by increasing the effective overlap between the optical field and the analyte region. Therefore, the APT configuration represents meaningful advancement toward compact, high-performance biosensors with realistic fabrication feasibility. A fundamental feature of such systems is the exceptional point (EP) a non-Hermitian degeneracy marking the phase transition between the PT-symmetric and PT-broken regimes at which the eigenvalues and eigenfunctions of the scattering matrix coalesce. At the EP, the reflection spectra exhibit a pronounced $\pi$-phase discontinuity [16, 17, 18, 19, 20]. In one-dimensional photonic systems, exceptional points are associated with unidirectional transparency, a phenomenon that substantially enhances the sensitivity of the optical response [21, 22].

PT-symmetric optical sensors have been extensively developed for a wide range of sensing applications, including the detection of liquids, gases, temperature variations, and biomedical markers. These sensors operate based on changes in the refractive index of analytes [23, 24, 25, 26, 27, 28, 29, 30, 31]. PT-symmetric structures exhibit several intriguing properties, such as anisotropic transmission resonance [32], power oscillations [33], optical transparency [34], and nonreciprocal propagation [35]. Early studies on PT-symmetric sensors primarily focused on one-dimensional systems, where bound states and the resonant phase condition determine the spectral positions of transmission peaks. The incorporation of PT symmetry in these systems leads to a transition from a single crossing point to a pair of exceptional points (EPs), resulting in unidirectional zero reflection [23].

A notable contribution by Zhang [24] introduced a PT-symmetric gas sensor that departed from traditional designs. This sensor measured the refractive index of gas samples through the transmittance height at the defect mode. In the field of non-invasive diagnostics, PT symmetry has enabled promising techniques for measuring glucose levels in the skin, addressing limitations associated with conventional passive sensing methods [25]. A recent study proposed a microcavity design for analyzing blood samples, leveraging blood plasma concentration and defect mode amplification. This design demonstrated high sensitivity and enhanced performance for medical sensing applications [26]. Zaky et al. [27] presented a PT-symmetric biosensor based on a one-dimensional photonic crystal composed of polymer doped with quantum dots and porous silicon (PSi) [36]. Their work revealed amplified

transmittance resonance peaks, enabling accurate detection of varying refractive indices [27]. Further research has explored the magnification of topological edge state peaks within photonic bandgaps [28] and the use of photoelastic effects in PT-symmetric composite structures for pressure sensing [29]. Additionally, a two-parameter PT-symmetric sensor was developed for dual monitoring of temperature and chemical substances [30]. Another study examined a defected PT-symmetric photonic crystal sensor operating in the terahertz regime to detect propylene glycol gas, where PT symmetry enhanced the resonant confined mode for improved detection [31]. Over the past decade, significant efforts have been made to develop optical biosensors based on photonic crystals, non-Hermitian platforms, and PT-symmetric configurations to enhance sensitivity and detection accuracy. Numerous studies have explored one-dimensional and multilayer structures incorporating graphene, quantum dots, or porous silicon to strengthen light–matter interaction and to tailor resonance conditions for cancer biomarker detection. Although these earlier works have demonstrated remarkable advances in sensitivity and miniaturization, most of them have focused on either conventional PT-symmetric or Hermitian designs without addressing the inherent trade-offs between gain–loss balance, fabrication tolerance, and practical implementation. A critical comparative review of recent PT-symmetric biosensing configurations highlights that current designs often suffer from limited tunability near the exceptional point (EP) and lack systematic optimization of porosity and structural thickness, which restricts their real-world applicability. Furthermore, only a few studies have investigated hybrid configurations that combine PT symmetry with material engineering to achieve both sensitivity enhancement and structural compactness as discussed in the comparative analysis of recent designs. However, despite these advances, challenges remain in balancing gain–loss distribution, minimizing structural thickness, and maintaining high fabrication tolerance. The present work addresses these challenges by proposing an augmented PT (APT)-symmetric one-dimensional photonic biosensor that merges design compactness with exceptional-point engineering for improved detection of cancerous tissues.

In this study, we investigate a one-dimensional photonic structure designed as a biosensor for the detection of cancer cells and tissues. The presence of augmented PT symmetry in the structure leads to distinctive optical phenomena. Using the transfer matrix method, we analyze the transmission and reflection components to identify exceptional points and determine the locations of bidirectional transparency [37, 38]. The novelty of this work lies in utilizing exceptional points and corresponding analyte refractive index values to distinguish cancerous cells and tissues. In structures with augmented PT symmetry, the layer thickness required to achieve exceptional points related to cancer is significantly reduced. This reduction in thickness and porosity ratio facilitates structural miniaturization and supports a more efficient minor sampling process. As a result, the proposed biosensor achieves enhanced efficiency and practicality for cancer detection through a compact and optimized design. Therefore, this study aims to design and analyze an augmented PT-symmetric photonic biosensor that not only achieves high sensitivity but also demonstrates structural miniaturization and practical manufacturability, aspects that have been scarcely addressed in earlier PT-symmetric biosensing literature.

The remainder of this paper is structured as follows: In the “Theoretical Approach” section, we detail the transfer matrix method, the concept of exceptional points, and the classification of normal versus abnormal tissues and cells, including their associated refractive indices. The

"Results and Analysis" section presents the key findings, demonstrating that cancerous tissues can be identified based on the analyte's refractive index at exceptional points. This section also emphasizes the benefits of structural miniaturization and the minor sampling method. The "Fabrication Feasibility and Experimental Prospects" section represents the feasibility of fabricating the proposed APT-symmetric structure. Finally, the "Conclusion" summarizes the major outcomes and implications of this study.

## Theoretical Approach

The schematic design of the proposed parity-time (PT)-symmetric microcavity biosensor is depicted in Fig. 1. The structure comprises multilayer stacks arranged as two symmetric photonic crystals positioned above and below a central sample layer. Each photonic crystal consists of alternating layers of porous silicon (PSi), gain (G), and loss (L) materials. The entire configuration is oriented along the Z-axis and exhibits PT symmetry with respect to the central analyte layer. The gain and loss layers, with respective thicknesses $d_G$ and $d_L$, are symmetrically arranged around the analyte layer, which has a thickness $d_s$ and a tunable refractive index $n_s$. The refractive indices of gain and loss layers, where silica is used as the host medium doped with quantum dots, can be described by the Lorentzian model [39, 26]:

$$n_{G(L)} = \sqrt{\varepsilon_0 + \frac{\alpha_{G(L)}\omega_0^2}{\omega_0^2 - \omega^2 - \omega\gamma i}} \tag{1}$$

Where $\varepsilon_{silica} = 1.5$ is the permittivity of the substrate material. The $\alpha_{G(L)}$ represents the related macroscopic Lorentz oscillation of gain and loss layer. So, $\omega_0 = 1.216\times10^{15}$ rad/s and $\omega$ represent the resonance frequency and the frequency of indices wave, respectively. $\gamma = 2.5\times10^{14}\,s^{-1}$ is the damping factor. It is noteworthy that for $\omega = \omega_0$ the imaginary parts of $n_{G(L)}$ have the opposite signs. The refractive index of porous silicon can be obtained from Bruggeman's relation [40]:

$$n_{PSi} = 0.5\sqrt{\Omega + \sqrt{\Omega^2 + 8n_{Si}^2 n_s^2}} \quad ; \quad \Omega = 3P\left(n_s^2 - n_{Si}^2\right) + \left(2n_{Si}^2 - n_s^2\right) \tag{2}$$

Where P, $n_s$, $n_{Si}$ are the porosity ratio and refractive indices of analyte sample and silicon, respectively. By using the transfer matrix method (TMM), the transmission and reflection spectra will be calculated. The electromagnetic wave at the right and left of interfaces can be related by transfer matrix as equation 3. Where the formation of total transfer matrix M can be expressed by the multiplication of the jth layer transfer matrix for whole q layers.

$$\begin{bmatrix} E' \\ H' \end{bmatrix} = M \begin{bmatrix} E \\ H \end{bmatrix} \quad ; \quad M = \begin{bmatrix} m_{11} & m_{12} \\ m_{21} & m_{22} \end{bmatrix} = \prod_{j=1}^{q} m_j \tag{3}$$

For TE polarization the transfer matrix for the jth layer can be expressed by equation 4.

$$m_j = \begin{bmatrix} \cos\delta_j & -\frac{i}{\eta_j}\sin\delta_j \\ -i\eta_j\sin\delta_j & \cos\delta_j \end{bmatrix} \quad ; \quad \eta_j = \sqrt{\frac{\varepsilon_0}{\mu_0}} n_j \cos\theta_j \ , \ \delta_j = \frac{2\pi}{\lambda} d_j n_j \cos\theta_j \tag{4}$$

Parameters $d_j$, $n_j$, and $\theta_j$ represents thickness, refractive index and incidence angle, respectively. The $\varepsilon_0$ and $\mu_0$ are the permittivity and the permeability of the vacuum. According to equation 5, on both sides of the reciprocal system the transmission beams are the same and obtained by the diagonal components of total transfer matrix. Meanwhile, Because of the non-reciprocity property, the components of the reflected beams were different from each other and expressed by the off-diagonal components of the total transfer matrix.

$$t = t_f = t_b = \frac{1}{M_{22}} \;\; ; \;\; r_f = \frac{M_{12}}{M_{22}} \;\; ; \;\; r_b = -\frac{M_{21}}{M_{22}} \tag{5}$$

In addition, the transmittance and reflectances can be calculated by: $T = |t|^2$, and $R_{f(b)} = |r_{f(b)}|^2$, respectively. Meanwhile, the scattering matrix for incident and scattered waves can be written as:

$$S = \begin{bmatrix} t_b & r_f \\ r_b & t_f \end{bmatrix} \tag{6}$$

The related eigenvalues can be given by: $\beta_{1,2} = t \pm \sqrt{r_f r_b}$. According to the conservation relation for spectra: $|T-1| = \sqrt{R_f R_b}$, exceptional points (EPs) are critical in understanding the transitions between PT-symmetric, and broken PT-symmetric. At an EP, the eigenvalues of the system coalesce, leading to significant changes in optical properties. In PT-symmetric regime, both gain and loss are balanced, leading to observable bidirectional transparency where light can pass through the system without reflection. While, in broken PT-symmetric regime, the balance of gain and loss is disrupted, causing reflection to occur and the system to lose its transparency. The transitions between these regimes can be precisely controlled by tuning structural parameters, which influence the location of EPs and the corresponding optical behavior. This control over EPs is pivotal for enhancing the sensitivity of biosensors, allowing for the detection of subtle changes in analyte refractive indices, critical for applications in early cancer diagnosis. This makes the structure highly sensitive to variations in the refractive index of the defect (analyte) layer. Additionally, due to the periodic arrangement of layers with contrasting refractive indices, photonic band gaps (PBGs) are formed, restricting wave propagation at certain wavelengths. The introduction of a defect layer within this stratified structure produces a resonant mode within the PBG. The refractive index of the defect layer acting as the analyte affects this resonance, allowing for various configurations in biosensing and biomedical applications. The primary performance metrics are sensitivity and limit of detection, defined as [41]:

$$\begin{aligned} S(\mathrm{nm/RIU}) &= \frac{\Delta\lambda_m}{\Delta n_s} \\ \mathrm{LoD(RIU)} &= \frac{\mathrm{FWHM}}{20S} \end{aligned} \tag{7}$$

where $\Delta\lambda_m$ is the resonance wavelength shift per unit change in analyte refractive index $\Delta n_s$. The parameter FWHM is the full width at half maximum of the resonance. By monitoring

changes in the analyte's refractive index, it becomes possible to diagnose a variety of diseases. As such, one-dimensional photonic crystals (1D-PCs) have emerged as simple, cost-effective, and precise biosensors. The position of the resonant peak directly corresponds to the refractive index of biological cells, enabling disease detection and classification. When normal and abnormal cells are exposed to the same electromagnetic source, they respond differently due to variations in refractive index. Abnormal cells, typically having higher protein content, exhibit higher refractive indices than normal cells. For instance, normal cells usually have a refractive index around 1.350, whereas benign and malignant cells range from 1.380 to 1.401. The eccentric growth of abnormal cells leads to the proliferation of cancer cells, a condition responsible for nearly one in six deaths globally. Cancer can spread to other organs and tissues and is often associated with infections caused by viruses such as hepatitis, human papillomavirus (HPV), and Epstein-Barr virus (EBV) [42, 43, 44, 45, 46, 47, 48, 49, 50, 51]. A comparative summary of typical refractive indices for healthy and cancerous cells is provided in Table 1.

**Table 1.** Refractive indices of healthy and cancerous cells.

| ***Cancer type*** | ***Cell name*** | | ***RI*** |
|---|---|---|---|
| **Liver cancer** | Primary stage | Healthy HC cell | **1.361** |
| | | Cancerous HC cell | **1.343** |
| | Secondary stage | Healthy LM cell | **1.345** |
| | | Cancerous LM cell | **1.347** |
| **Skin cancer** | Healthy basal cell | | **1.360** |
| | Cancerous basal cell | | **1.380** |
| **Blood cancer** | Healthy Jurkat cell | | **1.370** |
| | Cancerous Jurkat cell | | **1.390** |
| **Cervical cancer** | Healthy HeLa cell | | **1.368** |
| | Cancerous HeLa cell | | **1.392** |
| **Adrenal gland cancer** | Healthy PC12 cell | | **1.381** |
| | Cancerous PC12 cell | | **1.395** |
| **Breast cancer** | Healthy MDA-MB-231 cell | | **1.385** |
| | Cancerous MDA- MB-231 cell | | **1.399** |
| | Healthy MCF-7 cell | | **1.387** |
| | Cancerous MCF-7 cell | | **1.401** |

The human brain is a highly complex organ. This essential organ performs several critical functions, including sensory interpretation, movement, cognitive processing, and emotional regulation. According to data from the Brain Injury Association of America, approximately 2.6 million individuals sustain some form of brain injury each year. Brain lesions refer to areas of brain tissue that have been damaged due to disease or trauma. From the perspective of refractive index analysis, photonic crystal biosensors have shown promise in the early detection of both normal and abnormal cells [52, 53, 54, 55]. As indicated in Table 2, the refractive index varies significantly depending on the type of sample ranging from 1.333 for cerebrospinal fluid (CSF), the clear fluid surrounding the brain and spinal cord, to 1.483 for metastatic (cancerous) cells.

**Table 2.** Refractive indices of brain tissues.

| ***Brain tissues*** | | | ***Cell name*** | ***RI*** |
|---|---|---|---|---|
| **Normal tissues** | | | Gray matter | **1.395** |
| | | | Cerebrospinal fluid (CSF) | **1.333** |
| **Abnormal tissues** | Injured tissues | | Wall of solid brain | **1.341** |
| | | | Multi Sclerosis | **1.342** |
| | | | Oligodendroglioma | **1.353** |
| | Tumors and Cancers | Benign | White matter | **1.412** |
| | | | Low grade glioma | **1.432** |
| | | Malignant | Medulloblastoma | **1.441** |
| | | | Glioblastoma | **1.447** |
| | | | Lymphoma | **1.459** |
| | | | Metastasis | **1.483** |



## Results and Analysis

The proposed simple structure, illustrated in Fig. 1, consist of porous silicon, gain and loss layers arranged around a central analyte sample layer. Three distinct configurations are considered. The first structure ($S_1$) can be expressed as: $\mathbf{(PSi/G)^N/sample/(L/PSi)^N}$ , where the gain and loss layers sandwich the analyte layer symmetrically. The second structure ($S_2$), composed of: $\mathbf{(L/PSi)^N/sample/(PSi/G)^N}$, a reversed configuration compared to $S_1$. The third one ($S_3$), is a combinatorial structure that integrates both $S_1$ and $S_2$, with the analyte layer inserted at the center of a symmetric unit cell. In all configurations, N denotes the number of periodic unit cells. In $S_1$ and $S_2$, parity-time (PT) symmetry is maintained with respect to the central analyte layer. However, in $S_3$, PT symmetry is extended to the unit cells themselves, resulting in an augmented parity-time (APT) symmetry. For initial analysis, the layer thicknesses are set as follows: gain/loss layers 1020 nm, PSi layers 917 nm, and the analyte layer 1500 nm. The electromagnetic wave incident perpendicularly. The Lorentz oscillation of gain and loss layers are defined by: $\alpha_G = -2.3\times10^{-4}$, and $\alpha_L = 2.3\times10^{-4}$ [27, 55]. The refractive index of silicon is taken as 3.42, and the incident wavelength is 1550 nm. To ensure symmetry and layer consistency, the number of unit cells on either side of the analyte in $S_1$ and $S_2$ is set to N=3, while in $S_3$, the unit cells above and below the central unit cell are set to N=1. Unlike conventional PT-symmetric configurations where gain and loss are symmetrically within the unit cells, the augmented PT (APT) structure $S_3$ introduces symmetry distributed around the analyte. These internal and external symmetry coupling effectively halves the optical path required to reach the exceptional point, thereby reducing device thickness and enhancing field overlap with the analyte. Consequently, $S_3$ achieves both miniaturization and higher sensitivity without compromising fabrication feasibility.

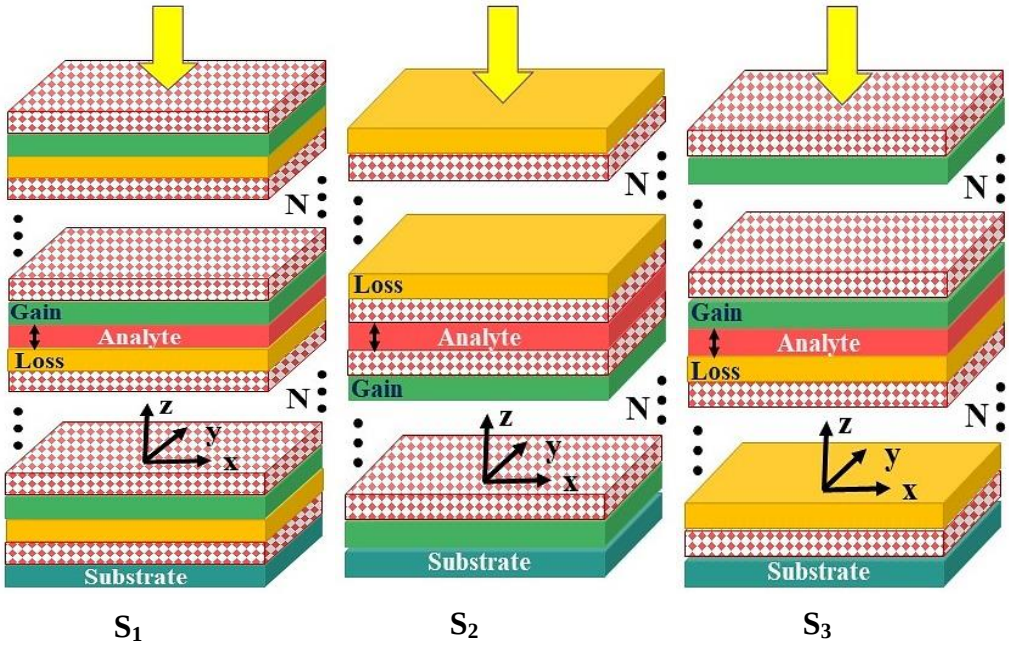


**Figure 1. Schematic representation of the proposed one-dimensional photonic biosensors.** Configurations $S_1$ and $S_2$ exhibit parity–time (PT) symmetry, while $S_3$ incorporates augmented PT (APT) symmetry. Each structure consists of alternating porous silicon (PSi), gain (G), and loss (L) layers surrounding the central analyte sample. The red dotted layers represent analyte-filled pores in PSi.

As a case study, we examine an analyte representing a healthy cell with a refractive index of 1.350, as previously noted. By carefully tuning the structural parameters, the resonant mode can be engineered to reach its maximum precisely at this refractive index. For Structure 1 ($S_1$), the transmission and reflection amplitudes as functions of the analyte's refractive index are presented in Fig. 2. The layer thicknesses are set according to the predefined values. The structure incorporates N = 3 unit cells on each side of the analyte layer, and the porosity ratio of the porous silicon is fixed at P = 57%.

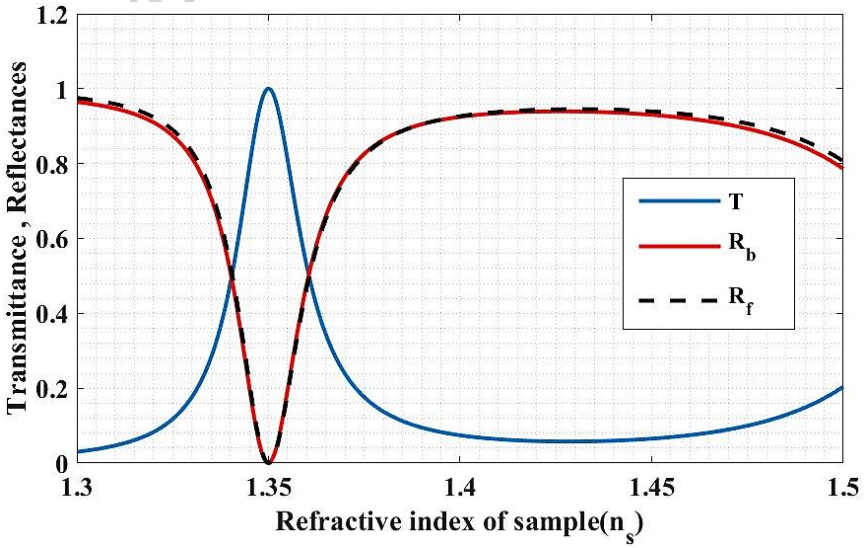

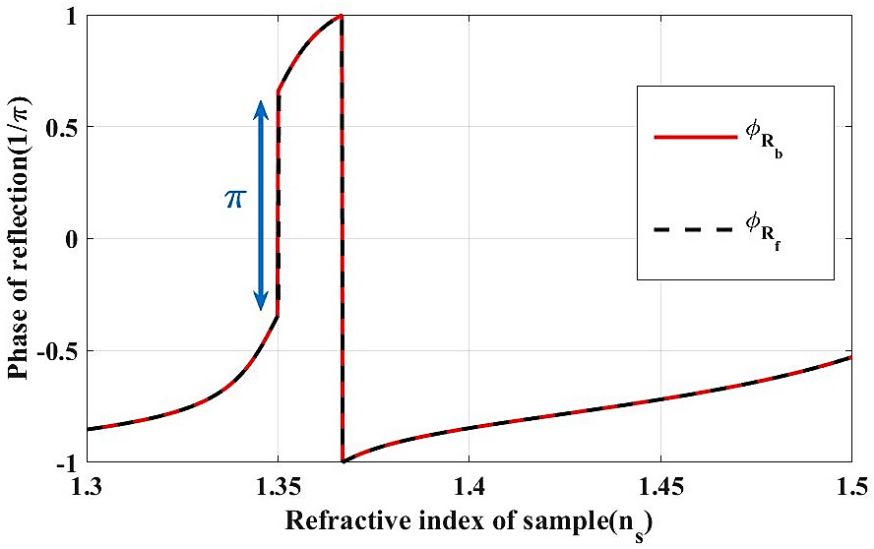


**Figure 2. Transmission and reflection characteristics of structure $S_1$.**
(Top) Transmission and reflection amplitudes as functions of the analyte refractive index ($n_s$). (Bottom) Forward and backward reflection phases showing π-phase discontinuity at the exceptional point (EP) corresponding to $n_s$ = 1.350. The calculations are performed for N = 3 and P = 57%.

By precisely tuning the parameters of all three structures, it is shown that the transmission attains its maximum value of unity when the refractive index is 1.350. At this point, both the forward and backward reflection components simultaneously reach their minimum values. In other words, when the analyte corresponds to a healthy cell, the resonant mode is fully excited, and the system exhibits bidirectional transparency effectively rendering it invisible at the specific refractive index associated with that cell type. At this same point, the forward and backward reflection phases experience a π-phase shift. Furthermore, although not illustrated here, the eigenvalues of the scattering matrix coalesce and become unimodular at this exceptional point.

Similarly, both healthy and unhealthy cells and tissues can be analyzed within the analyte layer. By optimizing the structural parameters, it is possible to accurately detect and distinguish cell and tissue types based on the refractive index at which the transmission peak occurs. This capability is essential for early diagnosis, with the potential to facilitate preventive measures and reduce the duration of treatment.

As shown in Tables 1 and 2, by varying the thickness of the porous silicon layers in structure $S_1$, the transmission can be maximized at refractive indices corresponding to liver cancer for example, in the case of primary-stage liver cancer (Hepatocellular Carcinoma (HC)) with a refractive index of 1.343, the optimal porous layer thickness is determined to be 921 nm, resulting in a transmission peak precisely at this value. Through parameter tuning, the system exhibits bidirectional transparency at the corresponding refractive index. Similarly, for the secondary stage of liver cancer (Liver Metastasis (LM)) which has a refractive index of 1.347, a porous layer thickness of 918.5 nm yields the maximum transmission. These results are depicted in Figure 3. The same optimization approach can be applied and validated for structures $S_2$ and $S_3$.

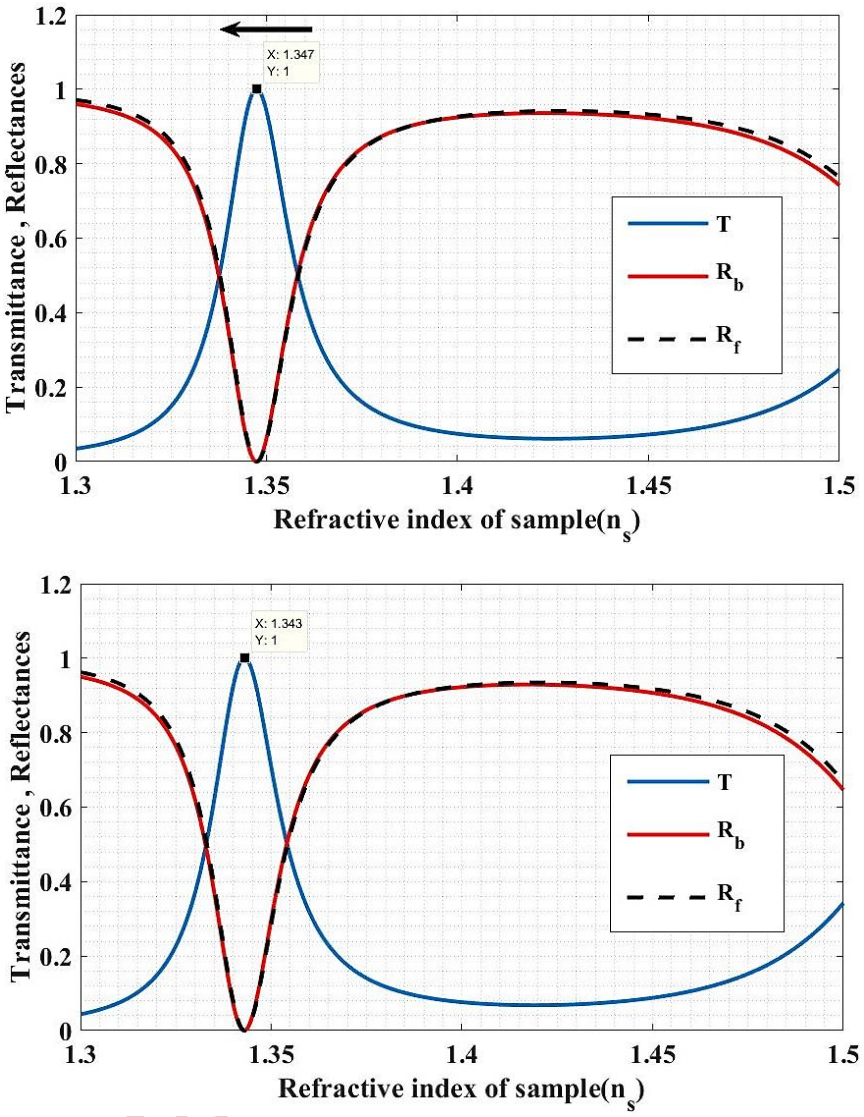


**Figure 3. Exceptional point locations for liver-related analytes.**
Transmission and reflection spectra for (top) Liver Metastasis ($n_s$ = 1.347, $d_{psi}$ = 918.5 nm) and (bottom) Hepatocellular Carcinoma ($n_s$ = 1.343, $d_{psi}$ = 921 nm). Bidirectional transparency occurs at the EP where transmission reaches unity.

To provide a more comprehensive insight into the optical response of the biosensor across various biological analytes, Figure 4 presents the transmittance spectra for representative cancerous cells and brain tissues. Each curve exhibits a distinct resonance wavelength whose position directly corresponds to the analyte's refractive index listed in Tables 1 and 2. The occurrence of sharp and narrow resonant peaks reflects the strong field confinement at the exceptional points. Notably, as the refractive index increases from 1.350 to 1.483, the resonance wavelength redshifts almost linearly, confirming that the designed photonic configuration preserves a one-to-one mapping between optical response and tissue type. This direct correlation forms the foundation for precise disease identification and demonstrates the capability of the miniaturized PT-symmetric structure to discriminate closely spaced refractive indices associated with malignant and benign tissues.

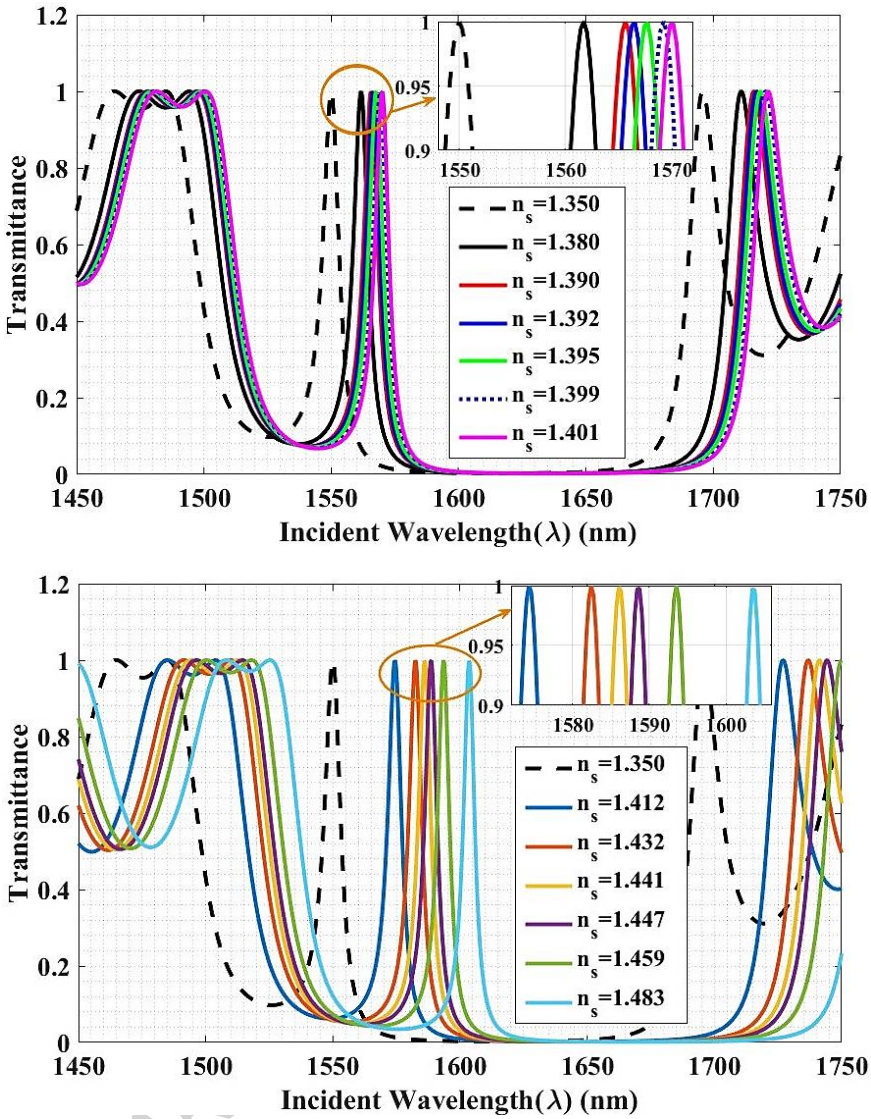


**Figure 4. Transmittance spectra for cancerous cells and brain tissues.**
Each curve corresponds to a distinct analyte refractive index listed in Tables 1 and 2. The inset shows a magnified view around the resonance wavelengths ($\lambda_m$), demonstrating the spectral shift associated with increasing $n_s$. The simulations were performed under normal incidence.

Table 3 summarizes the extracted resonance wavelengths ($\lambda_m$) corresponding to each analyte refractive index ($n_s$) in Figure 4. The nearly linear dependence yields an average sensitivity for the augmented PT-symmetric structure ($S_3$).

**Table 3.** Resonant wavelength versus analyte refractive index.

| $n_s$ | 1.350 | 1.380 | 1.390 | 1.392 | 1.395 | 1.399 | 1.401 | 1.412 | 1.432 | 1.441 | 1.447 | 1.459 | 1.483 |
|---|---|---|---|---|---|---|---|---|---|---|---|---|---|
| $\lambda_m$(nm) | 1550 | 1562 | 1565 | 1567 | 1568 | 1569 | 1571 | 1574 | 1582 | 1586 | 1588 | 1594 | 1603 |

The sensitivity of the proposed APT-symmetric biosensor was evaluated by monitoring the resonance wavelength shift in the transmission spectrum as the refractive index of the analyte layer was varied. Specifically, the transmission response was calculated using the transfer matrix method for successive refractive-index values corresponding to healthy and cancerous tissues. The resonance wavelength was extracted from the peak (or dip) position in the transmission curve, and the sensitivity was defined as equation 7. This approach enables

quantitative evaluation of the biosensor's response to minute refractive-index perturbations. In the APT configuration, the balanced gain–loss distribution and field localization near the exceptional point (EP) produce a stronger modulation of $\lambda_m$ for the same $\Delta n_s$, resulting in significantly enhanced sensitivity compared with conventional PT-symmetric structures. These results confirm that the sensing enhancement in the APT design originates from exceptional-point-assisted field amplification rather than mere geometrical modification. Figure 5 illustrates the influence of the porosity ratio (P) of the porous silicon layers on the biosensor's sensitivity (S) and limit of detection (LoD). A moderate porosity range yields an optimal trade-off between field localization and optical loss. For structure $S_3$, sensitivity increases sharply with decreasing P, reaching its maximum at P ≈ 58.5 %, while LoD achieves its minimum of $6.31\times10^{-5}$ RIU. In contrast, $S_1$ exhibits a slower variation and a higher LoD ($\sim1\times10^{-3}$ RIU). These results confirm that APT symmetry effectively enhances the overlap between the optical field and the analyte region, reinforcing the sensor's precision under realistic fabrication tolerances.

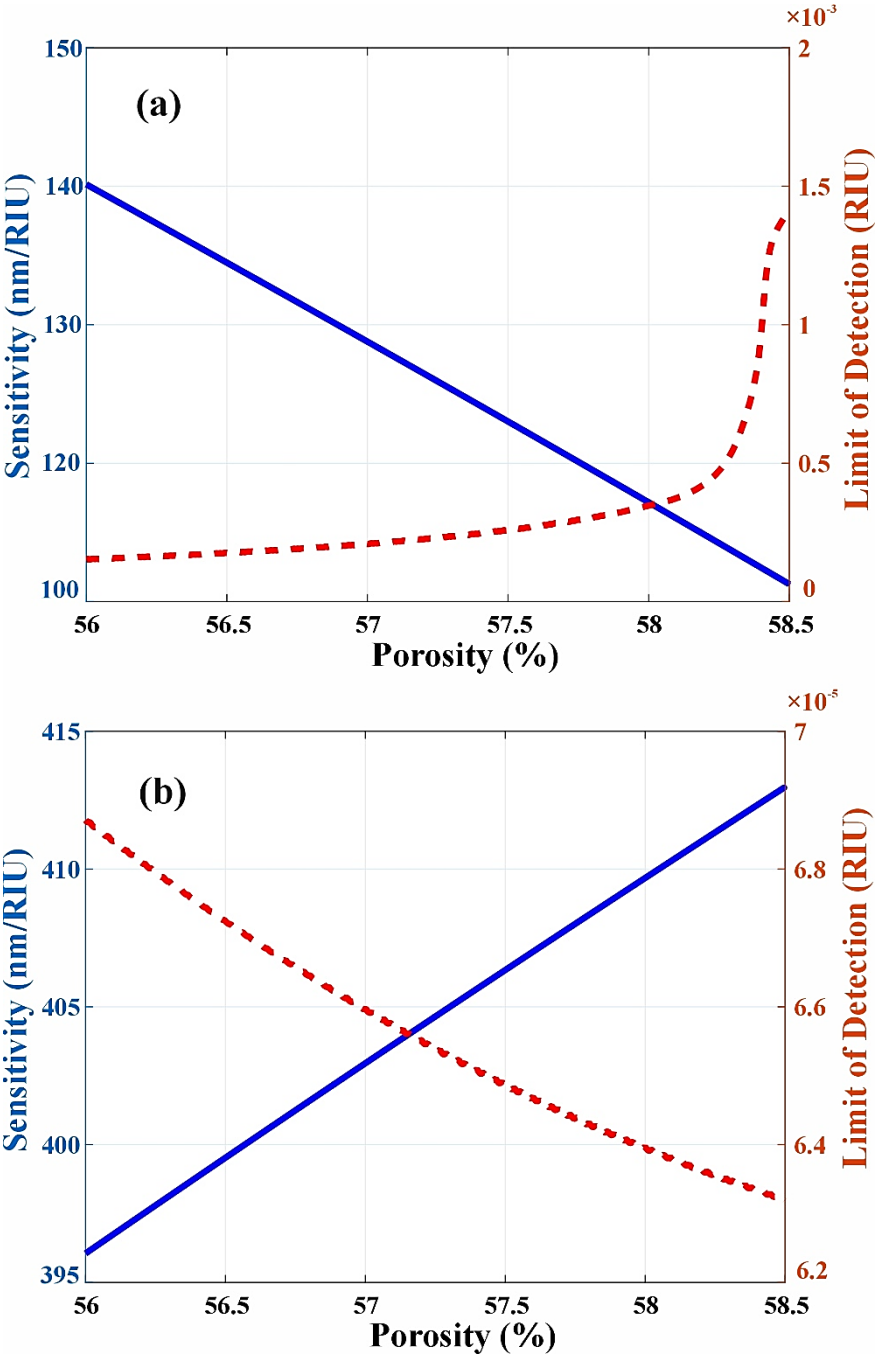


**Figure 5. Sensitivity (S) and limit of detection (LoD) versus porosity ratio.**
(a) Structure $S_1$ and (b) structure $S_3$. The S increases and LoD decreases with decreasing porosity.

To quantify the enhancement achieved by the proposed APT-symmetric design, several performance benchmarks were considered, including sensitivity, limit of detection. Among these, the APT configuration exhibited the highest sensitivity owing to the strong electromagnetic field confinement near the exceptional point, which amplifies even minute refractive-index variations of the analyte. The incorporation of both gain–loss balance and porous entry channels resulted in a dual enhancement mechanism that strengthens bidirectional transparency and minimizes energy dissipation. Consequently, the overall sensing efficiency was significantly improved compared to the PT-symmetric structures ($S_1$ and $S_2$). Furthermore, due to reduced layer thickness and optimized porosity, the proposed design offers superior fabrication tolerance and miniaturization, ensuring stable performance

under realistic experimental variations. These quantitative benchmarks collectively justify the superior operational efficiency of the proposed biosensor. Table 4 quantitatively compares the performance metrics of the three studied configurations. The augmented PT-symmetric design ($S_3$) achieves the highest sensitivity (≈ 413 nm/RIU) and the lowest detection limit, representing improvement relative to $S_1$ and $S_2$. This demonstrates that the APT configuration not only reduces the structural footprint but also significantly enhances analytical precision. The observed performance gain is primarily attributed to the hybridization of the forward and backward modes near the exceptional point, which maximizes energy confinement within the analyte layer.

**Table 4.** Performance metrics of biosensor structures ($S_1$-$S_3$).

| *Structures* / *Metrics* | $S_1$ | $S_2$ | $S_3$ |
|---|---|---|---|
| **Sensitivity (nm/RIU)** | 103 | 86 | 413 |
| **LoD (RIU)** | $2.23 \times 10^{-4}$ | $3.74 \times 10^{-4}$ | $6.31 \times 10^{-5}$ |

The observed trends in sensitivity and limit of detection can be directly linked to the position of the EP within the complex eigenvalue spectrum of the PT-symmetric system. Increasing the porosity of the Si layers effectively reduces the average refractive index of the periodic stack, thereby shifting the EP toward higher incident angles and weakening the field overlap between gain–loss regions. Conversely, reducing porosity enhances the refractive index contrast and strengthens modal coupling, resulting in a sharper resonance and higher sensitivity. Similarly, variations in layer thickness modify the optical path length and phase accumulation across each unit cell, which in turn alters the condition for mode coalescence at the EP. Optimal sensing occurs when the phase delay satisfies the half-wave condition, ensuring maximal energy confinement at the analyte interface. Quantitatively, the augmented PT configuration ($S_3$) demonstrates a substantial improvement over traditional PT designs. Specifically, the required layer thickness for achieving exceptional points is reduced by nearly 50%, while the porosity ratio decreases by approximately 10–15%. These reductions directly translate into a smaller device footprint and reduced fabrication complexity. Moreover, the enhanced field confinement observed in $S_3$ yields a fourfold increase in sensitivity compared to $S_1$ and $S_2$, confirming that miniaturization and performance enhancement can be achieved simultaneously. A unique characteristic not reported in earlier PT-symmetric biosensors [17, 31, 35]. To highlight the advantages of the proposed miniaturized APT-symmetric biosensor, Table 5 provides a benchmark comparison with previously reported PT- and non-PT-based photonic structures. The present design exhibits the highest sensitivity and comparable or superior LoD while maintaining a compact geometry. This comparison validates the novelty of the proposed approach and its relevance to practical biomedical diagnostics. Moreover, the compatibility of porous silicon and quantum-dot gain media suggests straightforward integration into existing nanofabrication workflows, supporting experimental realization. These improvements indicate the feasibility of clinical deployment for real-time biomarker sensing.

**Table 5.** Comparative study with previously reported photonic biosensors.

| *Structure/Configuration* | *Sensitivity (nm/RIU)* | *LoD(RIU)* | *Reference* | *Year* |
|---|---|---|---|---|
| A gas sensor in IR regime, using a PhC with defect | 270 | $\sim 10^{-4}$ | Baghdouche et al. [56] | 2020 |
| Defective 1D PhC with a defect cavity | 102 | $3.50 \times 10^{-5}$ | Aly et al. [57] | 2021 |
| 1D PT-symmetric PhC with a central defect layer | 227 | $5.10\times 10^{-6}$ | Yi et al. [26] | 2021 |
| A defective PhC waveguide for cancerous blood detection | 344 | --- | Abohassan et al. [58] | 2021 |
| Nonlinear delta-function PhC for detecting sodium iodide solution | 410 | $8 \times 10^{-4}$ | Mehaney et al. [59] | 2022 |
| 1D PhC of metal/cavity/ dielectric with Hybrid Tamm plasmon | 259 | --- | Jena et al. [60] | 2022 |
| 1D PhC of ZnSe/Nb2O5 /BK7 as a tunable wide bandstop filter | 81 | $90 \times 10^{-6}$ | Abohassan et al. [61] | 2022 |
| 1D miniaturized APT-symmetric PhC with a central defect layer | 413 | $6.31 \times 10^{-5}$ | This Work | |

By varying the thickness of the porous layers and utilizing the distinct refractive indices of cancerous cells and tissues listed in Table 3, the system is designed to diagnose diseases at the points where bidirectional transparency is achieved.

**Table 3.** Porous layer thickness variations at exceptional points for different tissues.

| ***Porous medium thicknesses $d_{PSi}$ (nm)*** | | | ***RI at EP*** | ***Cancer cells and tissues*** |
|---|---|---|---|---|
| ***$S_1$*** | ***$S_2$*** | ***$S_3$*** | | |
| **899** | **928** | **297.3** | **1.380 →** | **Skin cancer** (Cancerous basal cell) |
| **893** | **922.5** | **294** | **1.390 →** | **Blood cancer** (Cancerous Jurkat cell) |
| **891.5** | **919.5** | **292.5** | **1.392 →** | **Cervical cancer** (Cancerous HeLa cell) |
| **890** | **921.5** | **293.5** | **1.395 →** | **Adrenal gland cancer** (Cancerous PC12 cell) |
| **887** | **917.5** | **291.3** | **1.399 →** | **Breast cancer** (Cancerous MDA-MB-231 cell) |
| **886** | **916.5** | **290.5** | **1.401 →** | **Breast cancer** (Cancerous MCF-7 cell) |
| **879** | **910** | **286.8** | **1.412 →** | **Brain cancer** (Benign-White matter) |
| **865** | **898.5** | **280** | **1.432 →** | **Brain cancer** (Benign-Low grade glioma) |
| **859** | **893.5** | **276.5** | **1.441 →** | **Brain cancer** (Malignant-Medulloblastoma) |
| **854.5** | **890** | **274.5** | **1.447 →** | **Brain cancer** (Malignant-Glioblastoma) |
| **846** | **882.6** | **270** | **1.459 →** | **Brain cancer** (Malignant-Lymphoma) |
| **828** | **868.5** | **261** | **1.483 →** | **Brain cancer** (Malignant-Metastasis) |

A comparison of the results for structures $S_1$ and $S_2$, as presented in Table 3, reveals that the required porous layer thickness in $S_1$ is consistently smaller than that in $S_2$. This indicates that $S_1$ offers improved sensor performance. Thinner layers are particularly beneficial in biosensor design, enhancing compactness and fabrication efficiency. Consequently, $S_1$ represents a more practical option for optimizing porous layer thickness in the detection of exceptional points (EPs) and, by extension, various diseases.

As previously discussed, both $S_1$ and $S_2$ exhibit parity-time (PT) symmetry. However, the system demonstrates increased efficiency under augmented parity-time (APT) symmetry, as implemented in structure $S_3$. The introduction of APT symmetry in $S_3$ results in a reduction of the required porous layer thickness by approximately one-third, thereby contributing to a significant miniaturization effect an essential advantage in biosensor applications. This underscores the superior performance of $S_3$ compared to $S_1$ and $S_2$.

Following this, the impact of the porosity ratio of the porous layers is investigated. The number of unit cells is set to 3 for $S_1$ and $S_2$, and 1 for $S_3$, with the porous layer thickness fixed at 917 nm across all structures. All other parameters remain unchanged. As shown in Table 4 variations in the porosity ratio lead to shifts in the position of the maximum

transmission peak, aligning with the refractive indices of different cancer cells and tissues. This enables precise identification of disease types.

**Table 4.** Porosity variations at exceptional points for different tissues.

| ***The ratio of the pores P (%)*** | | | ***RI at EP*** | ***Cancer cells and tissues*** |
|---|---|---|---|---|
| ***$S_1$*** | ***$S_2$*** | ***$S_3$*** | | |
| **59** | **55.72** | **47.15** | **1.380 →** | **Skin cancer** (Cancerous basal cell) |
| **59.7** | **56.4** | **47.65** | **1.390 →** | **Blood cancer** (Cancerous Jurkat cell) |
| **59.9** | **56.5** | **47.75** | **1.392 →** | **Cervical cancer** (Cancerous HeLa cell) |
| **60.1** | **56.7** | **47.9** | **1.395 →** | **Adrenal gland cancer** (Cancerous PC12 cell) |
| **60.4** | **56.92** | **48.1** | **1.399 →** | **Breast cancer** (Cancerous MDA-MB-231 cell) |
| **60.55** | **57.1** | **48.18** | **1.401 →** | **Breast cancer** (Cancerous MCF-7 cell) |
| **61.4** | **57.8** | **48.8** | **1.412 →** | **Brain cancer** (Benign-White matter) |
| **63** | **59.2** | **49.9** | **1.432 →** | **Brain cancer** (Benign-Low grade glioma) |
| **63.75** | **59.85** | **50.4** | **1.441 →** | **Brain cancer** (Malignant-Medulloblastoma) |
| **64.3** | **60.3** | **50.8** | **1.447 →** | **Brain cancer** (Malignant-Glioblastoma) |
| **65.34** | **61.21** | **51.5** | **1.459 →** | **Brain cancer** (Malignant-Lymphoma) |
| **67.45** | **63** | **53** | **1.483 →** | **Brain cancer** (Malignant-Metastasis) |

According to Table 4, the porosity ratio in $S_3$ is lower than in $S_1$ and $S_2$. This lower porosity facilitates detection and identification with smaller sample volumes and enhanced accuracy. The ability to operate with minimal sampling offers significant advantages, aligning with current research trends that emphasize the development of diagnostic methods requiring reduced sample quantities. Although some medical researchers advocate for large-scale sampling to improve statistical reliability, such approaches may introduce greater variability and reduce the overall validity of results. In contrast, smaller sample sizes can help minimize confounding factors and enhance the precision of measurements. Considering both the reduced thickness and lower porosity ratio, structure $S_3$ emerges as a more practical and efficient choice compared to $S_1$ and $S_2$.

Another important parameter influencing system performance is the thickness of the gain and loss layers. As presented in Table 5, varying this thickness allows the maximum transmission to be tuned to match the refractive indices of specific cancerous cells and tissues. In these evaluations, the porous layer and sample layer thicknesses are fixed at 917 nm and 1500 nm, respectively. The number of unit cells remains unchanged, and the porosity ratio is held constant at P = 57%. The incident electromagnetic wave is normal to the structure and has a wavelength of 1550 nm.

**Table 5.** Gain/loss layer thickness variations at exceptional points for different tissues.

| ***Gain & Loss medium thicknesses $d_{G(L)}$ (nm)*** | | | ***RI at EP*** | ***Cancer cells and tissues*** |
|---|---|---|---|---|
| ***$S_1$*** | ***$S_2$*** | ***$S_3$*** | | |
| **1000.5** | **1050** | **526** | **1.380 →** | **Skin cancer** (Cancerous basal cell) |
| **994** | **1035** | **519** | **1.390 →** | **Blood cancer** (Cancerous Jurkat cell) |
| **992.5** | **1032** | **517** | **1.392 →** | **Cervical cancer** (Cancerous HeLa cell) |
| **990.5** | **1028** | **515** | **1.395 →** | **Adrenal gland cancer** (Cancerous PC12 cell) |
| **988** | **1022** | **512** | **1.399 →** | **Breast cancer** (Cancerous MDA-MB-231 cell) |
| **986.5** | **1019** | **511** | **1.401 →** | **Breast cancer** (Cancerous MCF-7 cell) |
| **979** | **1000** | **502** | **1.412 →** | **Brain cancer** (Benign-White matter) |
| **965** | **963** | **486** | **1.432 →** | **Brain cancer** (Benign-Low grade glioma) |
| **958.6** | **940** | **479** | **1.441 →** | **Brain cancer** (Malignant-Medulloblastoma) |
| **953.8** | **928** | **474** | **1.447 →** | **Brain cancer** (Malignant-Glioblastoma) |
| **954** | **900** | **463.5** | **1.459 →** | **Brain cancer** (Malignant-Lymphoma) |
| **926.8** | **845** | **443** | **1.483 →** | **Brain cancer** (Malignant-Metastasis) |

As shown in Table 5, the thickness of the gain and loss layers required to achieve maximum transmission at the refractive indices associated with various cancer cells and tissues is consistently smaller in structure $S_1$ compared to $S_2$, up to a refractive index of 1.432. However, for the analysis of malignant brain tissue cells, $S_2$ offers a distinct advantage due to its reduced layer thickness in that specific range. Importantly, structure $S_3$ demonstrates a significant miniaturization effect, with the required thickness of the gain and loss layers reduced by approximately 50%.

Subsequently, the thickness of the analyte (sample) layer was varied to determine the corresponding maximum transmission values and to observe the phenomenon of bidirectional transparency at the relevant refractive indices. In this analysis, the thicknesses of the porous and gain/loss layers were fixed at 917 nm and 1050 nm, respectively, with a porosity ratio of 57%. As presented in Table 6, adjusting the sample layer thickness enables the accurate identification and diagnosis of different cancer cell types and tissues

**Table 6.** Sample layer thickness variations at exceptional points for different tissues.

| ***Sample medium thicknesses $d_s$ (nm)*** | | | ***RI at EP*** | ***Cancer cells and tissues*** |
|---|---|---|---|---|
| ***$S_1$*** | ***$S_2$*** | ***$S_3$*** | | |
| **1445** | **1542** | **418** | **1.380 →** | **Skin cancer** (Cancerous basal cell) |
| **1427** | **1522** | **365** | **1.390 →** | **Blood cancer** (Cancerous Jurkat cell) |
| **1423** | **1517** | **356** | **1.392 →** | **Cervical cancer** (Cancerous HeLa cell) |
| **1417** | **1510** | **343** | **1.395 →** | **Adrenal gland cancer** (Cancerous PC12 cell) |
| **1410** | **1502** | **323** | **1.399 →** | **Breast cancer** (Cancerous MDA-MB-231 cell) |
| **1407** | **1498** | **316** | **1.401 →** | **Breast cancer** (Cancerous MCF-7 cell) |
| **1386** | **1474** | **265** | **1.412 →** | **Brain cancer** (Benign-White matter) |
| **1348** | **1431** | **195** | **1.432 →** | **Brain cancer** (Benign-Low grade glioma) |
| **1330** | **1410** | **170** | **1.441 →** | **Brain cancer** (Malignant-Medulloblastoma) |
| **1318** | **1397** | **155** | **1.447 →** | **Brain cancer** (Malignant-Glioblastoma) |
| **1293** | **1370** | **125** | **1.459 →** | **Brain cancer** (Malignant-Lymphoma) |
| **1240** | **1315** | **77** | **1.483 →** | **Brain cancer** (Malignant-Metastasis) |

Table 6 indicates that the thickness of the analyte layer in structure $S_1$ is smaller than that in $S_2$. Consistent with previous findings, the exceptional point is more optimally positioned when the incident wave first interacts with the porous layer, thereby making $S_1$ more favorable for the detection of cancer cells and tissues. However, the results for structure $S_3$ are particularly noteworthy; it requires a significantly thinner analyte layer compared to both $S_1$ and $S_2$. This pronounced miniaturization effect is advantageous for implementing low-volume sampling techniques.

In summary, the enhanced sensitivity and reduced detection limit of the APT-symmetric configuration originate from its superior modal coupling near the exceptional point. Structural parameters such as porosity and thickness govern the exact location of this point in the complex frequency plane, and their optimization ensures maximal interaction between optical gain and loss, which is the fundamental mechanism behind the observed performance enhancement.

## Fabrication Feasibility and Experimental Prospects

Although the current investigation is primarily theoretical, the proposed PT- and APT-symmetric biosensor designs are compatible with existing nanofabrication techniques. The porous silicon layers can be produced via electrochemical anodization, where the porosity and thickness are precisely controlled through the current density and etching time. In practical terms, a tolerance of ±2% in layer thickness or porosity results in less than 0.5 nm deviation in the resonance wavelength, which remains well within the detection resolution of standard optical spectrometers. The implementation of gain and loss media can be achieved using silica matrices doped with semiconductor quantum dots, as demonstrated in several experimental studies [43, 60]. The optical gain level can be tuned through quantum-dot concentration and external optical pumping, while the corresponding loss is introduced by controlled absorption in the complementary layer to maintain PT balance. Although maintaining a perfectly balanced gain–loss profile is experimentally challenging, previous works have shown that near-PT-symmetric conditions are sufficient to preserve the exceptional-point phenomena and bidirectional transparency [16, 21]. Moreover, the proposed miniaturized APT configuration significantly reduces the total thickness, making it compatible with standard integrated photonic platforms. The structure can be deposited on silicon or BK7 substrates using layer-by-layer sputtering or chemical vapor deposition techniques. The low thermal budget required for porous silicon formation ensures compatibility with microfluidic integration, enabling future on-chip biosensing applications. Overall, the proposed biosensor is not merely a theoretical model but a practically feasible nanophotonic design, capable of being realized using well-established semiconductor and photonic fabrication methods.



## Conclusion

In summary, a one-dimensional non-Hermitian photonic biosensor based on augmented parity–time (APT) symmetry has been proposed and numerically analyzed for the precise detection of healthy and cancerous tissues. The optimized APT-symmetric configuration ($S_3$) exhibits outstanding sensing performance with a maximum **sensitivity of 413 nm/RIU**, and a **limit of detection (LoD) of 6.31 × $10^{-5}$ RIU**, outperforming conventional PT-symmetric counterparts ($S_1$ and $S_2$). These enhancements originate from exceptional-point–induced field localization and balanced gain–loss interaction, which collectively strengthen spectral resolution and sensing accuracy. The proposed design achieves high detection precision while maintaining a reduced optical footprint, making it well-suited for low-volume biosample analysis and CMOS-compatible fabrication using porous silicon and quantum-dot–doped materials. Looking forward, integrating this APT-symmetric biosensor with microfluidic systems could enable real-time, label-free cancer biomarker monitoring. Moreover, extending the concept to two-dimensional photonic architectures and performing experimental validation using real biological samples represent promising directions toward translating this theoretical framework into practical biomedical sensing applications.

## Data availability

The datasets generated and/or analyzed during the current study are available from the corresponding author upon reasonable request.

## References


[1] J. L. Santos and F. Farahi, Handbook of Optical Sensors, CRC Press, 2015.

[2] P. S. Nunes, N. A. Mortensen, J. P. Kutter and K. B. Mogensen, "Refractive index sensor based on a 1D photonic crystal in a microfluidic channel," *Sensors*, vol. 10, pp. 2348-2358, 2010.

[3] E. Yablonovitch, "Photonic crystals: Semiconductors of light," *Sci. Am.*, vol. 285, pp. 46-55, 2001.

[4] E. Beheiry, M. Liu, V. Fan and S. Levi, "Sensitivity enhancement in photonic crystal slab biosensor," *Opt. Express*, vol. 18, pp. 22702-22714, 2010.

[5] N. A. Vanyushkin, I. M. Efimov and A. H. Gevorgyan, "The sensitivity of refractive index sensors based on defected 1D photonic crystals: an analytical approach," *Phys. Scr.*, vol. 99, no. 105521, 2024.

[6] H. K. Baghbadorani and J. Barvestani, "Effect of uniaxial strain on the performance of one-dimensional graphene Fibonacci photonic crystal biosensor," *J. Lightwave Thechol.*, vol. 36, no. 5406, 2018.

[7] H. Kaviani and J. Barvestani, "Photonic crystal based biosensor with the irregular defect for detection of blood plasma," *Applied Surface Science*, vol. 599, no. 153743, 2022.

[8] H. A. Elsayed, A. G. Mohamed, A. M. El-Sherbeeny, A. H. Aly, M. R. Abukhadra, W. A. Zoubi and A. Mehaney, "Improved performance of temperature sensors based on the one-dimensional topological photonic crystals comprising hyperbolic metamaterials," *Scientific Reports*, vol. 14, no. 19733, 2024.

[9] D. Dash, J. Saini, A. K. Goyal and Y. Massoud, "Exponentially index modulated nanophotonic resonator for high-performance sensing applications," *Scientific Reports*, vol. 13, no. 1431, 2023.

[10] A. K. Goyal, A. Kumar and Y. Massoud, "Performance analysis of heterostructure-based topological nanophotonic sensor," *Scientific Reports*, vol. 13, no. 19415, 2023.

[11] C. M. Bender and S. Boettcher, "Real spectra in non-Hermitian Hamiltonians having PT symmetry," *Phys. Rev. Lett.*, vol. 80, no. 24, 1998.

[12] C. M. Bender, "Introduction to $\mathcal{PT}$-symmetric quantum theory," *Contemporary Phys.*, vol. 46, pp. 277-292, 2005.

[13] C. M. Bender, "Making sense of non-Hermitian Hamiltonians," *Rep. Prog. Phys.*, vol. 70, pp. 974-1018, 2007.

[14] C. M. Bender, "PT-symmetry in quantum physics: from a mathematical curiosity to optical experiments," *Europhys. News*, vol. 47, pp. 17-22, 2016.

[15] A. Mohammadpour, J. Barvestani and A. S. Vala, "Extraordinary directional optical properties of a parity-time symmetric one-dimensional photonic lattice," *Opt. Commun.*, vol. 500, no. 127342,

2021.

[16] S. K. Ozdemir, S. Rotter, F. Nori and L. Yang, "Parity-time symmetry and exceptional points in photonics," *Nat. Mat. 2019, 18, 783-798.*

[17] A. Krasnok, N. Nefedkin and A. Alu, "Parity-Time Symmetry and Exceptional Points," *IEEE Antennas & Propagation Magazine,* vol. 63, no. 6, 2021.

[18] W. D. Heiss, "Exceptional points of non-Hermitian operators," *J. Phys. Math. Gen. 37, 2455-2464 (2004).*

[19] A. Mohammadpour, J. Barvestani and A. S. Vala, "Comprehensive study of singular points in a PT-symmetric Thue-Morse multilayer," *Physica Scripta,* vol. 97, no. 125501, 2022.

[20] J. Barvestani and A. Mohammadpour, "The effect of the centric graphene layer on the exceptional points of parity-time symmetric photonic crystals," *Optical and Quantum Electronics,* vol. 56, no. 880, 2024.

[21] Z. Lin, H. Ramezani, T. Kottos, H. Cao and D. N. Christodoulides, "Unidirectional invisibility induced by PT-symmetric periodic structures," *Phys. Rev. Lett.*, vol. 106(21), no. 213901, 2011.

[22] M. Sarisaman, "Unidirectional reflectionlessness and invisibility in the TE and TM modes of a PT-symmetric slab system," *Phys. Rev. A,* vol. 95, 013806, 2017.

[23] D. Zhao, Y. Shen, Y. Zhang, X. Zhu and L. Yi, "Bound states in one-dimensional acoustic parity-time-symmetric," *Physics Letters A,* vol. 380, pp. 2698-2702, 2016.

[24] Y. Zhang and Y. Fang, "Gas sensor based on parity-time-symmetry structure," *Journal of Nanophotonics,* vol. 12(3), no. 036005, 2018.

[25] Y. J. Zhang, H. Kwon, M. A. Miri, E. Kallos, H. Cano-Garcia, M. S. Tong and A. Alu, "Noninvasive Glucose Sensor Based on Parity-Time Symmetry," *Physical Review Applied,* vol. 11, no. 044049, 2019.

[26] L. Yi and C. Li, "Simulation Research on Blood Detection Sensing with Parity-Time Symmetry Structure," *Crystals,* vol. 11, no. 1030, 2021.

[27] Z. A. Zaky, S. Alamri, V. D. Zhaketov and A. H. Aly, "Refractive index sensor with magnified resonant signal," *Scientific Reports,* vol. 12, no. 13777, 2022.

[28] A. A. Ameen, M. Al-Dossari, Z. A. Zaky and A. H. Aly, "Studying the effect of quantum dots and parity-time symmetry on the magnification of topological edge state peak as a pressure sensor," *Synthetic Metals,* vol. 292, no. 117233, 2023.

[29] Z. A. Zaky, M. Al-Dossari, A. Sharma and A. H. Aly, "Effective pressure sensor using the parity-time symmetric photonic crystal," *Physica Scripta,* vol. 98, no. 035522, 2023.

[30] X. Huang and Z. Meng, "Two-parameter Optical Sensing Based on Multilayer Parity-time-symmetric Structure," *Academic Journal of Science and Technology,* vol. 5, no. 1, 2023.

[31] Z. A. Zaky, M. Al-Dossari, V. D. Zhaketov and A. H. Aly, "Defected photonic crystal as propylene glycol THz sensor using parity-time symmetry," *Scientific Reports,* vol. 14, no. 23209, 2024.

[32] L. Ge, Y. D. Chong and A. D. Stone, "Conservation relations and anisotropic transmission resonances in one-dimensional PT-symmetric photonic heterostructures," *Phys. Rev. A*, vol. 85, no. 023802, 2012.

[33] A. Regensburger, C. Bersch, M. A. Miri, G. Onishchukov, D. N. Christodoulides and U. Peschel, "Parity–time synthetic photonic lattices," *Nature*, vol. 488, pp. 167-171, 2012.

[34] Y. Zhang, X. Yang, F. Tang, X. Wang, D. Deng, H. Liu and Z. Wei, "Singular systematic phases, transparencies, and invisibility produced by parity-time symmetric Thue-Morse optical waveguide networks," *Results in physics*, vol. 30, no. 104763, 2021.

[35] C. E. Ruter, K. G. Makris, R. El-Ganainy, D. N. Christodoulides, M. Segev and D. Kip, "Observation of parity-time symmetry in optics," *Nat. Phys.*, vol. 6, pp. 192-195, 2010.

[36] V. Lehmann, Electrochemistry of silicon: instrumentation, science, materials and applications, Weinheim: WILEY-VCH Verlag GmbH, 2002.

[37] T. G. Mackay and A. Lakhtakia, The transfer matrix method in electromagnetics and optics, Morgan & Claypool, 2020.

[38] J. Barvestani and A. Mohammadpour, "Tunable and giant spatial Goos–Hänchen shifts in a parity-time symmetric Cantor photonic crystals incorporated with a centered graphene layer," *Physica Scripta*, vol. 98, no. 055511, 2023.

[39] V. Klimov, A. Mikhailovsky, S. Xue, A. Malko, J. Hollingsworth, C. Leatherdale, H. Eisler and M. Bawendi, "Optical Gain and Stimulated Emission in Nanocrystal Quantum Dots," *Science*, vol. 290, no. 314, 2000.

[40] L. Canham, Handbook of Porous Silicon, Springer, 2020.

[41] J. Homola, "Surface plasmon resonance sensors for detection of chemical and biological species," *Chemical Reviews*, vol. 108(2), pp. 462-493, 2008.

[42] N. R. Ramanujam, I. S. Amiri, S. A. Taya, S. Olyaee, R. Udaiyakumar, A. P. Pandian, K. S. J. Wilson, P. Mahalakshmi and P. P. Yupapin, "Enhanced sensitivity of cancer cell using one dimensional nano composite material coated photonic crystal," *Microsystem Technologies*, 2018.

[43] A. Bijalwan, B. K. Singh and V. Rastogi, "Analysis of one-dimensional photonic crystal based sensor for detection of blood plasma and cancer cells," *Optik*, vol. 226, no. 165994, 2021.

[44] T. Parvin, K. Ahmed, A. M. Alatwi and A. N. Z. Rashed, "Differential optical absorption spectroscopy-based refractive index sensor for cancer cell detection," *Optical Review* , vol. 28, pp. 134-143, 2021.

[45] A. Panda, P. D. Pukhrambam, F. Wu and W. Belhadj, "Graphene-based 1D defective photonic crystal biosensor for real-time detection of cancer cells," *Eur. Phys. J. Plus*, vol. 136, no. 809, 2021.

[46] C. Malek, M. Al-Dossari, S. K. Awasthi and A. H. Aly, "High Performance Biosensor for Detection of the Normal and Cancerous Liver Tissues Based on 1D Photonic Band Gap Material Structures," *Sensing and Imaging*, vol. 24, no. 27, 2023.

[47] A. H. Aly, B. A. Mohamed, M. Al-Dossari, S. K. Awasthi, E. Fouad and A. F. Amin, "Ultra-high

sensitive cancerous cells detection and sensing capabilities of photonic biosensor," *Scientific Reports*, vol. 13, no. 19524, 2023.

[48] B. Karki, A. S. Alsubaie, P. Sarkar, M. Sharma and N. B. Ali, "Detection of Skin, Cervical, and Breast Cancer Using Au–Ag Alloy and WS2-Based Surface Plasmon Resonance Sensor," *Plasmonics*, 2024.

[49] M. F. Nayan, M. A. Raihan, M. H. Fuad, N. A. Zaman, T. Ahmed and R. R. Mahmud, "A high-performance biosensor based on one-dimensional photonic crystal for the detection of cancer cells," *Optical and Quantum Electronics* , vol. 56, no. 1968, 2024.

[50] A. Molaei-Yeznabad and H. Bahador, "Refractive Index-Based Optimized Ternary Photonic Crystal Biosensor for Ultra Precise Detection of Cancer Cells," *Sensing and Imaging*, vol. 26, no. 36, 2025.

[51] A. H. Aly and Z. A. Zaky, "Ultra-sensitive photonic crystal cancer cells sensor with a high-quality factor," *Cryogenics*, vol. 104, no. 102991, 2019.

[52] W. M. Nouman, S. E. A. El-Ghany, S. M. Sallam, A. F. B. Dawood and A. H. Aly, "Biophotonic sensor for rapid detection of brain lesions using 1D photonic crystal," *Optical and Quantum Electronics*, vol. 52, no. 287, 2020.

[53] C. Malek, M. Al-Dossari, S. K. Awasthi, Z. S. Matar, N. S. A. El-Gawaad, W. Sabra and A. H. Aly, "Employing the Defective Photonic Crystal Composed of Nanocomposite Superconducting Material in Detection of Cancerous Brain Tumors Biosensor: Computational Study," *Crystals*, vol. 12, no. 540, 2022.

[54] N. A. Mohammed, O. E. K. E.-S. M. El-Rabaie and A. A. Khalaf, "Brain tumors biomedical sensor with high-quality factor and ultra-compact size based on nanocavity 2D photonic crystal," *Alexandria Engineering Journal*, vol. 64, pp. 527-540, 2023.

[55] C. Malek, S. A. O. Abdallah, S. K. Awasthi, M. A. Ismail, W. Sabra and A. H. Aly, "Biophotonic sensor for swift detection of malignant brain tissues by using nanocomposite YBa2Cu3O7/dielectric material as a 1D defective photonic crystal," *Scientific Reports*, vol. 13, no. 8115, 2023.

[56] L. Kassa-Baghdouche and E. Cassan, "Mid-infrared gas sensor based on high-Q/V point-defect photonic crystal nanocavities," *Opt. Quantum Electron.*, vol. 52, 2020.

[57] A. H. Aly, S. K. Awasthi, D. Mohamed, Z. S. Matar, M. Al-Dossari and A. F. Amin, "Study on a one-dimensional defective photonic crystal suitable for organic compound sensing applications," *RSC Adv.*, vol. 11(52), pp. 32973-32980, 2021.

[58] K. M. Abohassan, H. S. Ashour and M. M. Abadla, "A 1D photonic crystal-based sensor for detection of cancerous blood cells," *Opt. Quantum Electron.*, vol. 53, pp. 1-14, 2021.

[59] A. Mehaney, M. M. Abadla and H. A. Elsayed, "Biosensors based on novel nonlinear delta-function photonic crystal comprising weak nonlinearities," *Sci. Reports*, vol. 12, no. 17674, 2022.

[60] S. Jena, R. B. Tokas, S. Thakur and D. V. Udupa, "Rabi-like splitting and refractive index sensing with hybrid Tamm plasmon-cavity modes," *J. Phys. D: Appl. Phys.*, vol. 55, no. 175104, 2022.

[61] K. M. Abohassan, H. S. Ashour and M. M. Abadla, "Tunable wide bandstop and narrow bandpass filters based on one-dimensional ternary photonic crystals comprising defects of silver nanoparticles in water," *J. Phys. Chem. Solids*, vol. 161, no. 110484, 2022.

**Acknowledgments**
This work is based upon research funded by Iran National Science Foundation (INSF) and Supreme Council of Science, Research and Technology (SCSRT) under project No. 4023866.

**Funding**
This work is based upon research funded by Iran National Science Foundation (INSF) and Supreme Council of Science, Research and Technology (SCSRT) under project No. 4023866.

**Author contributions**
A.M. conceived the research idea, performed the computational analysis, interpreted the results, and wrote the manuscript. A.M., A.S.V., and J.B. reviewed and edited the manuscript. All authors read and approved the final version of the manuscript.

**Competing interests**
The authors declare that they have no known competing financial interests or personal relationships that could have appeared to influence the work reported in this paper.

**Additional information**
Correspondence and requests for materials should be addressed to A.M.